Advanced Materials Interfaces

ADVANCED MATERIALS INTERFACES Open Access

www.advmatinterfaces.de

RESEARCH ARTICLE OPEN ACCESS

Overlapping Nanostacks Enable Direct Printing of Organic LEDs

Stefan Lux[1] | Jannik Schlindwein[1] | Martina Plank[2] | Klaus-Martin Reichert[3] | Liane Koker[3] | Maria Rosa[4] | Momina Amir[4] | Benjamin Weber[1] | Erich Müller[5] | Alexander Welle[6] | Nadezda Kuznetsova[4] | Michael Kraft[4] | Yolita M. Eggeler[5] | Laura K. Weber[1] | Daniela Mattes[1] | Ulrich Gengenbach[3] | Mareen Stahlberger[1] | Jan G. Korvink[1] | Frank Breitling[1] | Dario Mager[1]

[1]Karlsruhe Institute of Technology - Institute of Microstructure Technology (KIT), Eggenstein-Leopoldshafen, Germany | [2]Karlsruhe Institute of Technology - Soft Matter Synthesis Laboratory - Institute for Biological Interfaces 3 (IBG-3-SML), Germany | [3]Karlsruhe Institute of Technology - Institute for Automation and Applied Informatics (KIT), Eggenstein-Leopoldshafen, Germany | [4]Department of Electrical Engineering (Micro and Nano Systems) KU Leuven – University of Leuven, Leuven, Belgium | [5]Karlsruhe Institute of Technology - Laboratory for Electron Microscopy (KIT), Karlsruhe, Germany | [6]Karlsruhe Institute of Technology – Karlsruhe Nano Micro Facility (KNMFi) and Institute of Functional Interfaces, Eggenstein-Leopoldshafen, Germany

Correspondence: Dario Mager (dario.mager@kit.edu)

Received: 3 June 2025 | **Revised:** 27 September 2025 | **Accepted:** 20 October 2025

Keywords: additive manufacturing | laser-induced forward transfer | nanolayer | OLED

ABSTRACT

A custom-built laser-induced forward transfer (LIFT) setup was developed to fabricate multimaterial organic light emitting diode (OLED) stacks under ambient laboratory conditions without the use of a cleanroom or encapsulation. The process enables precise control of layer thickness through parameter tuning as confirmed by vertical scanning interferometry (VSI), yielding smooth and homogeneous layers with surface roughness values down to 2.78 nm. The process achieves tunable thicknesses between 19 nm and 45 nm, while the lateral resolution is limited to about 100 µm. A three-layer OLED stack (total thickness ≈ 90 nm) was printed and structurally characterized using focused ion beam scanning electron microscopy (FIB-SEM) and time-of-flight secondary ion mass spectrometry (ToF-SIMS), revealing distinct, well-defined layer boundaries. First functional tests demonstrated electroluminescence at 580 nm with an operational lifetime of at least 20 min. Despite the lack of encapsulation, the OLEDs remained stable under ambient conditions with a shelf life of up to 9 days. These results confirm the potential of LIFT as a scalable and precise tool for the additive manufacturing of flexible thin-film devices such as OLEDs, solar cells and fuel cells.

1 | Introduction

Since the early 2000s, electronic systems have rapidly advanced, driven by shorter innovation cycles, higher performance requirements and miniaturization [1]. This has created a constant demand for new products and manufacturing methods. Technologies like surface mount technology (SMT) [2] and system-on-a-chip [3] have been key milestones that represent today's standard solutions [4]. Additive manufacturing, an established technology in industrial production and still a significant as well as dynamic field of research, offers the advantages of flexibility in production, speed and cost-efficiency, and may replace or complement existing technologies [5, 6].

While research has made progress in various areas, inkjet printing has been established for the printing of a variety of materials. In the area of electronic engineering printed interconnects, actuators, sensors, and electronic devices are already being realized at the microscale [7–10].

Inkjet printing offers significant advantages over traditional additive manufacturing techniques, such as screen printing and aerosol jet printing, including high flexibility, low material consumption, and the capability to deposit complex geometries without physical contact [11]. However, several challenges remain: ink parameters must be precisely matched to the machine and the substrate surface must be compatible with the selected inks [12]. In the field of printed electronics, specific material properties are crucial to ensure proper component functionality. Among conventional techniques, screen printing is widely used due to its simplicity, scalability and high material purity, but it typically offers limited resolution in the range of 20 μm to 100 μm [11]. Inkjet printing, on the other hand, provides improved spatial resolution and enables the deposition of more complex geometries. However, it remains restricted to the microscale, and printing structures with dimensions below 100 nm—as required in high-precision applications—remain a significant challenge [12]. When the printing of electronics is scaled down to the nanoscale, further requirements are placed on the system. Surface effects become increasingly dominant, and printing systems must enable precise control over feature dimensions, material placement and layer thickness–capabilities that only a few techniques provide, such as two-photon polymerization (Nanoscribe) or electrohydrodynamic jet printing [13]. However, these methods face limitations including low throughput, complex process conditions, and high equipment costs, making them less suitable for large-scale industrial applications [6]. Consequently, there is a growing demand for alternative techniques that combine high resolution with scalability and broad material compatibility. This paper introduces LIFT as a potential solution or complement to existing additive manufacturing technologies. Originally developed in the 1990s, LIFT has seen significant growth since 2010 [14] and has branched into several subfields. Today, a variety of setups exist, specialized for transfer of a wide range of materials, including solids, liquids, and even living cells [15–19]. LIFT technology is currently in the process of becoming a versatile tool across multiple disciplines, offering a promising platform for high-throughput screening [20–23].Common to all LIFT techniques is a laser directed onto a donor substrate coated with a transfer material, a patch of which is then partially detached and accelerated toward a receiving substrate. Among the most promising extensions of this technology are blister-actuated LIFT (BA-LIFT) and dynamic release layer (DRL) variants, which offer improved control over transfer accuracy [24] (see Figure 1). While DRL-based methods improve accuracy, they can also cause unwanted effects when used for sensitive modules due to shockwave propagation [25]. Additional variants exist and are listed in the review by Chen et al. [25], along with their respective advantages and disadvantages [14]. These advantages make BA-LIFT not only a versatile technique, but also a strong candidate for industrial-scale applications. A scalable technique that reliably prints thin-film systems with nanometer z-precision and minimal material limitations would be highly promising for LED fabrication. To date, the fabrication of micro LED arrays has been limited by the challenge of integrating RGB pixels on the same wafer. As a result, current methods rely on the deterministic assembly of micro LED chips from different substrates [25]. LIFT could play a major role in the fabrication of micro LED arrays due to the advantage of parallelization with multiple lasers, and the direct transfer of modules. It was already shown that working micro LEDs can be transferred with LIFT and thus represent a real-world application [26, 27]. While micro LED integration is still emerging, similar transfer techniques have been successfully used in OLED fabrication. Recent studies report the transfer of complete, prefabricated OLED stacks, moved from donor to receiver substrate, a process known as transfer printing [28–31]. Using blister-actuated (BA) LIFT for the transfer minimizes the risk of damaged or misplaced modules. It also presents a way of shielding the OLED materials from elevated temperatures during the transfer [32]. In contrast to transfer printing approaches used for OLED fabrication a bottom-up process can be employed, in which each layer is successively built using LIFT (see Figure 1c). Using the BA-LIFT technology with the bottom-up principle offers greater design flexibility in the production of OLEDs, making it a promising approach for material screenings and iterative development cycles. In BA-LIFT [15, 24, 33] (see Figure 1a), the donor material is coated onto a polyimide film. Upon laser irradiation, the polyimide absorbs the energy and locally expands, pressing the donor material into contact with the acceptor substrate, where it adheres and forms a thin layer. The setup used in this work uses glass slides as the acceptor substrate and was shown to work with high precision for the printing of polymers as frozen solids, as demonstrated in previous studies [34, 35]. In both studies, the polymer S-LEC served not only as a precisely structured material dot on the nanometer scale, but also was used as a carrier material for transferring other substances, such as amino acids or dyes. Beyond these works, BA-LIFT processes have also been explored for the transfer of fluids, utilizing two primary mechanisms: direct laser absorption, leading to bubble formation within the ink, or laser-induced jet formation via interaction with an intermediate layer [36, 37]. These approaches expand the versatility of BA-LIFT but remain mostly focused on polymer-based or liquid-phase materials [24].

This work demonstrates how BA-LIFT is employed to print organic material layers with a thickness in the nanometer range, a lateral resolution of approximately 100 μm and how thickness and homogeneity of these layers can be controlled via the process parameters. In contrast to the transfer printing approach, printing an OLED using the bottom-up process is not limited by orthogonal processing or complex coating processes. The layer-by-layer (LbL) printing process results in a functional OLED, and the optimal printing parameters were identified by the measurement of individual layers and subsequent optimization. The structural quality (thickness, roughness and homogeneity) of the stack is characterized by FIB-SEM, ToF-SIMS, and VSI. A complete OLED stack composed of hole transport layer (HTL), emissive layer (EML) and electron transport layer (ETL), was fabricated by successive BA-LIFT printing steps, forming a multilayer architecture that enabled light emission after electrical addressing. As this is the first investigation of the LbL system, the focus is on the printing process. Nonetheless, first investigations of optical and electrical properties to confirm general applicability in the field of OLEDs were carried out.

2 | Results and Discussion

2.1 | Printing of Thin Layers

The generation of homogeneous thin layers with variable thickness and optimized surface roughness is essential for the

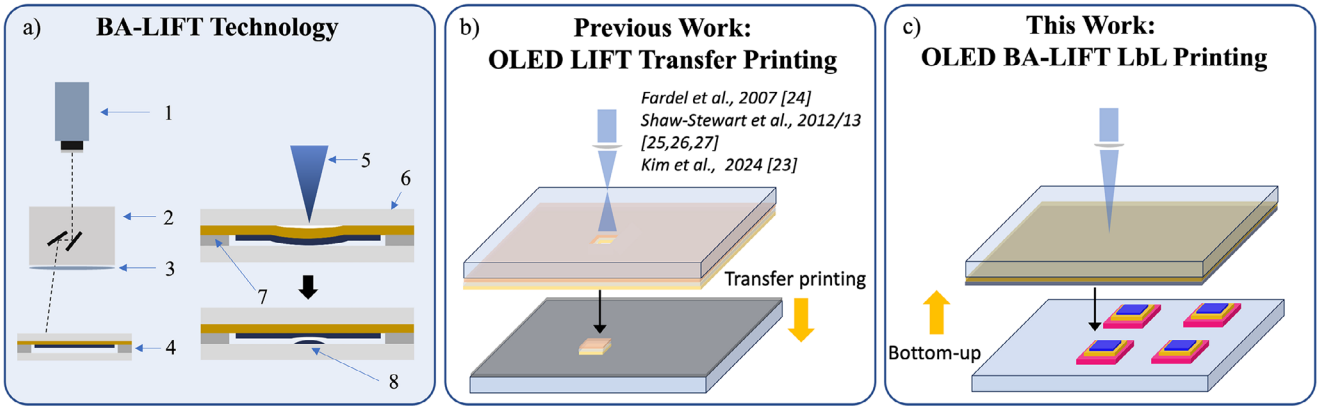

FIGURE 1 | BA-LIFT techniques for OLED fabrication. a) General functional diagram of the BA-LIFT process, showing the focused laser beam (5) that induces blister formation and enables the transfer of a material dot (8). Additional components: (1) Laser source, (2) Laser scanhead, (3) F-Theta lens, (4) Donor-acceptor slides, (6) Glass slide, (7) Spacer. b) Previous work: OLED transfer printing. c) This work: Layer-by-layer (LbL) bottom-up approach for OLED printing.

bottom-up fabrication process of OLEDs. Therefore, the development of suitable printing techniques is crucial for device fabrication as well as for potential high-throughput material screening. BA-LIFT technology has been shown to be capable for the printing of single dots in previous works [34, 35, 38]; this work demonstrates that the LIFT process can also be applied and optimized to produce continuous and homogeneous OLED layers with a target thickness from 1 nm to 100 nm and minimized roughness, enabling reliable layer integration in multilayer device structures. The adaptation of the process was initially developed with the S-LEC LIFT printing technology using a styrene acrylate copolymer, S-LEC PLT 7552, followed by a transfer and optimization for OLED materials, which is the primary focus of this work.

Previous studies have already examined the dimensions of the transferred dot as a function of laser power and exposure time. These studies demonstrated that both the height and the lateral size of each individual dot can be adjusted by variation of laser power and exposure time. A reduction in laser power or exposure time led to a decrease in the transferred volume, resulting in smaller dot height and lateral dimensions [34]. To allow the printing of surfaces, an overlap of the individual printed dots was targeted in order to generate more continuous and smooth surfaces. For this purpose, the distance from dot center to dot center, the pitch, was systematically varied and values of 80 µm, 60 µm, and 8 µm were investigated. As shown in Figure 2, insufficient overlap—especially at larger pitch values—resulted in inhomogeneous structures with height fluctuations of up to 30 nm and gaps with no transferred material. By gradually reducing the pitch, a smoother transition between dots was achieved. A pitch of 8 µm, which is drastically smaller than the approximate dot size of 100 µm, created a high degree of overlap and enabled the formation of continuous surfaces. To compensate for the resulting increase in local energy input, the laser power was reduced to 70 mW and the exposure time was shortened to 1 ms. This optimized set of parameters was used to fabricate the structure shown in Figure 2c.

Further reduction of the pitch was found to significantly decrease the reproducibility of individual dot transfers. This is due to the expanding polyimide blister which extends laterally far beyond the size of the printed material dot. Although laser exposure lasts only a few milliseconds, the blister continues to expand for up to 70 ms [34], causing a temporal and spatial overlap of successive transfers. As a result, overlapping blisters interfere with each other during subsequent transfers, leading to uncontrolled deposition. Consequently, the expansion is no longer an isolated event but becomes a continuous process along the laser direction. This behavior has also been described by Munoz–Martin et al. [39] for LIFT printing of liquid silver ink, where pressure bubbles are released toward existing cavities at small pitches, disrupting the transfer. Our observations at a pitch of ≈ 60 µm show similar interference effects, despite differences in the material system. Process monitoring as described by Das et al. [40] could facilitate even more optimization of the process parameters as well as a more detailed understanding.

In this section it was shown that homogeneous surface printing was successfully achieved using the standard BA-LIFT approach with a S-LEC polymer donor layer. The optimized parameters for continuous, smooth deposition were a pitch of 8 µm, a laser power of 70 mW and an exposure time of 1 ms. These settings enabled sufficient dot overlap without triggering undesired interactions between expanding blisters.

2.2 | Printing of Layers with Variable Height

For OLED applications, precise control of layer thickness is even more critical than surface roughness, as it plays a key role in device functionality. Since the small molecules used in OLED fabrication often differ significantly from polymers in terms of physical and chemical properties, process parameters must be specifically optimized for each material. In this study, the control over the layer thickness is illustrated using the model substance bathophenanthrolin (BPhen).

Two parameters were identified to control the thickness, the concentration of the material on the donor slide and the laser parameters. Variation of the donor solution concentration

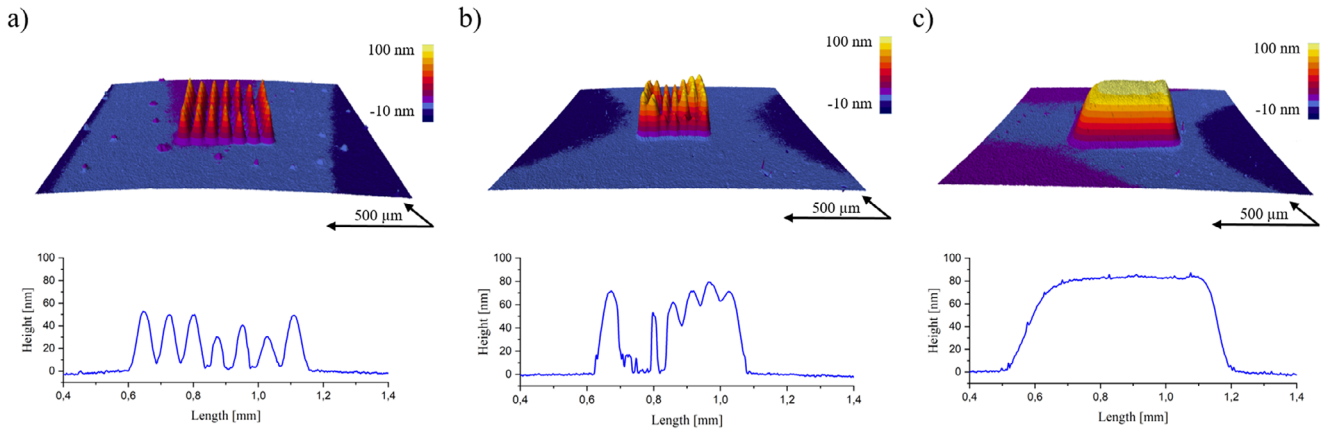

FIGURE 2 | Printing with different pitches with S-LEC material results in a) dots beginning to overlap (80 µm, 150 mW, 10 ms); b) fused dots forming a polymer layer which is not plane (60 µm, 150 mW, 7 ms); c) fused dots with homogeneous height forming a plane layer (8 µm, 70 mW, 1 ms).

revealed that higher concentrations result in increased donor loading in the film and, in consequence, higher thickness of the transferred layers on the acceptor, while laser parameters remained constant. In Figure 3a, the height of the printed layers for different concentrations is shown. VSI revealed that the layer thickness increases from 20 nm at the lowest BPhen concentration ($4\,mgmL^{-1}$) to 140 nm at the highest concentration ($30\,mgmL^{-1}$), showing an approximately linear trend up to $12mg\,mL^{-1}$, followed by a saturation effect at higher concentrations. Increasing layer thickness may lead to more laser-induced kinetic energy being absorbed in the viscous layers, causing a reduction in the amount of material effectively transferred. Possibly the saturation is also related to incomplete transfer of material.

Further adjustment of layer height and improvement of printing quality was achieved by variation of the laser parameters power and exposure time. Starting from a defined standard setting (8 µm pitch, 70 mW laser power, 2 ms exposure time), variations in these parameters affected not only the transfer quality but also resulted in measurable changes in layer thickness. Figure 3b–d displays topographic images and corresponding line profiles of the printed surfaces obtained under varied laser settings, with the material concentration kept constant. These variations led to an increase in layer thickness of approximately 20 nm when either the laser power was raised from 70 mW to 80 mW or the exposure time was extended from 2 ms to 3 ms. It is important to note that the surface roughness was strongly affected by these changes. The lowest R_a value of 2.78 nm ± 0.25 nm was obtained under the standard conditions (70 mW, 2 ms), which were also used for subsequent OLED fabrication. Extending the exposure time to 3 ms led to a moderate increase in roughness (R_a = 3.29 nm ± 0.27 nm). However, increasing the laser power to 80 mW caused a significant rise in roughness to R_a = 6.08 nm ± 1.24 nm, as is clearly visible in the surface topography. These results underline the necessity to carefully balance energy input and exposure time to achieve both, sufficient layer thickness and minimal surface roughness. The described protocol is applied in the following for the fabrication of an OLED, in order to achieve the layer thicknesses required for proper device operation with a minimized surface roughness. In comparison to the pixel transfer method by LIFT with DRL, the roughness was significantly reduced using BA-LIFT, representing a clear improvement of the LIFT process [30].

In this chapter, two approaches were identified to control the layer thickness: variation of the concentration of the donor coating solution and adjustment of the laser parameters. In addition, the adjustment of the laser parameters could be used for the optimization of the surface roughness.

3 | Fabrication and Characterization of Micro-OLED Arrays

In OLED printing, it is crucial to enable the controlled flow of charge carriers in the desired sequence, from the ITO substrate to the top electrode. This requires a precise preparation of the substrate and a functional layer stack composed of distinct nanolayers to ensure optimal device performance. For this purpose, a specially structured printing substrate was developed on the basis of glass slides with a 100 nm ITO layer. The bottom electrode must be transparent to allow the transmission of the emitted light in this direction. The nano 3D printer is designed to handle samples the size of microscope slides. The developed layout enables printing of 20 ITO pads on one slide, as shown in Figure 4a. Each pad is connected to an ITO contact pad at the side of the slide to allow for external contacting of the anode. While stacking the OLED layers in a tower-like configuration might appear to be a straightforward approach, it presents significant challenges in establishing contact to the upper electrode without causing short circuits through the entire stack. Therefore, a staggered pyramid structure is chosen, as shown in Figure 4b. This design facilitates the connection to the anode ITO surface and enables charge carrier flow through the printed layer stack to the aluminum cathode. To ensure proper operation of the OLED, the top electrode is deposited by evaporation of aluminum in combination with a shadow mask. The shadow mask, fabricated by laser cutting a steel foil, defines the geometry of the cathode and ensures precise patterning.

In general, OLEDs comprise an EML in which the recombination of electrons and holes causes electroluminescence. The EML is sandwiched between ETL and HTL that enable the migration of

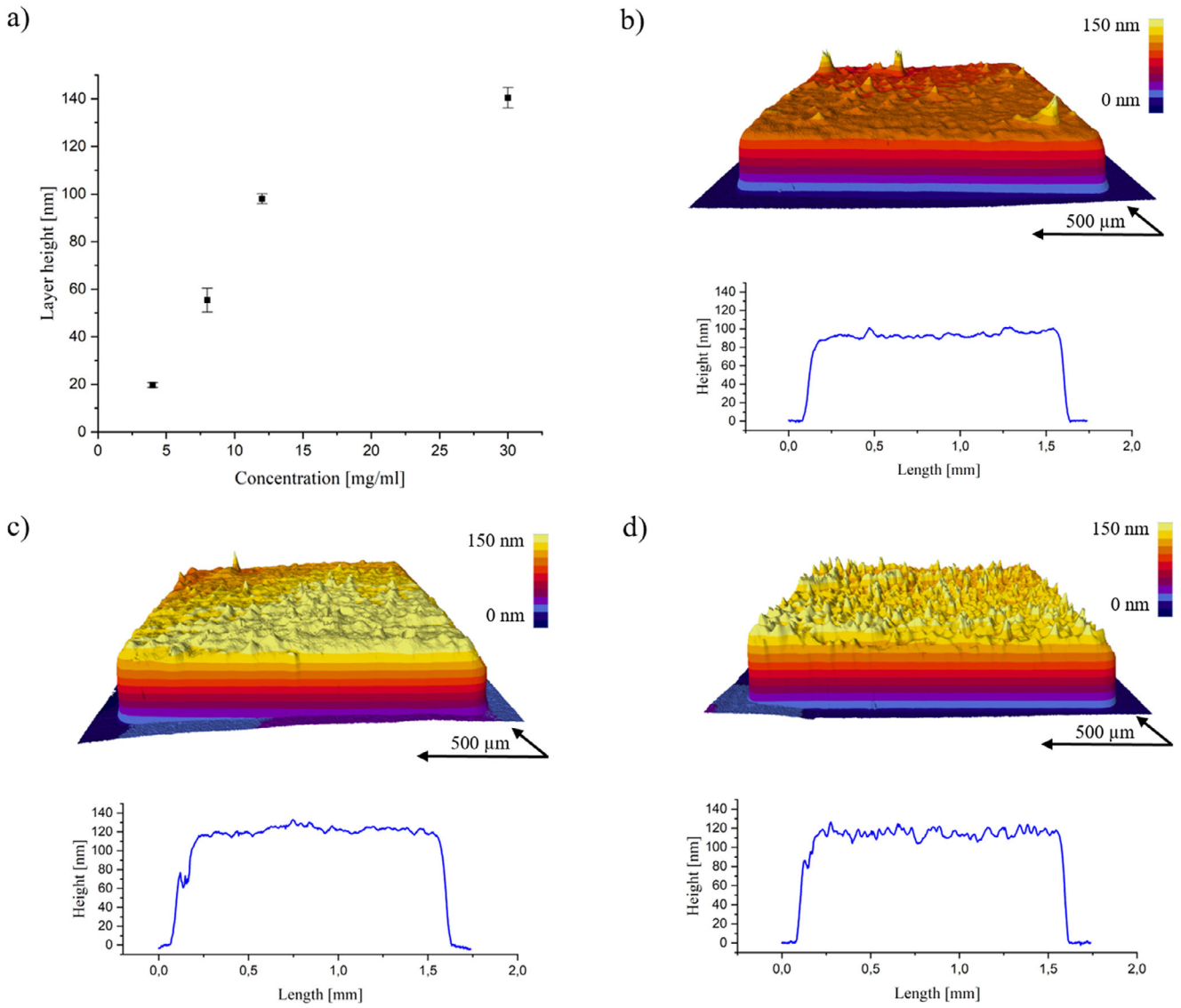

FIGURE 3 | a) Height distribution of printed Bphen layers in relation to the material concentration. Bars indicate standard deviation. Transfer of Bphen under different laser conditions was investigated while keeping the concentration of the donor material constant at 12 mgmL^{-1}. Topographic images display the surface features, while line profiles indicate thickness variations for laser powers and exposure times of b) 70 mW, 2 ms c) 70 mW, 3 ms, and d) 80 mW, 2 ms.

charge carriers from cathode and anode to the EML. To ensure better charge mobility, more complex OLED architectures often include additional layers, e.g., electron and hole injection layers. Since the fabrication of the first OLED in 1987 [41], a wide variety of materials has been explored for each individual layer. In OLEDs, all layers consist of organic or sometimes metal organic compounds which can be small molecules or polymer-based materials. In this work, we selected a small set of organic small molecules for the individual layers since the printing of small molecules through BA-LIFT has been demonstrated in previous works [35] and the optimization of the respective printing parameters is more straightforward than for polymeric materials. It should be noted that the layering of purely organic materials with similar polarity and solubility is often very challenging in OLED fabrication as solution-based printing methods often compromise the layer integrity. Thus, these materials would be difficult to layer using standard fabrication techniques. The OLEDs in this study were printed using different combinations of HTL materials (TCTA and TPD) and fluorescent emitters (Rubrene and Alq_3) in conjunction with the ETL material BPhen. Each material layer was transferred in its pure form, point by point, using the laser-based printing process and was subsequently analyzed by VSI to determine layer characteristics. This method avoids the use of solvents and helps maintain the integrity of the previously deposited layers. Functionality testing was carried out to determine suitable transfer parameters as shown in Table 1. For some materials the transferred material quantity is lower due to specific material properties, making a second printing pass necessary to reach the desired height, which is indicated by the number of prints in the table. For each subsequent print a new donor slide was used. Each material showed a slightly different printing behavior which makes an individual optimization of printing parameters and donor film coating procedure necessary.

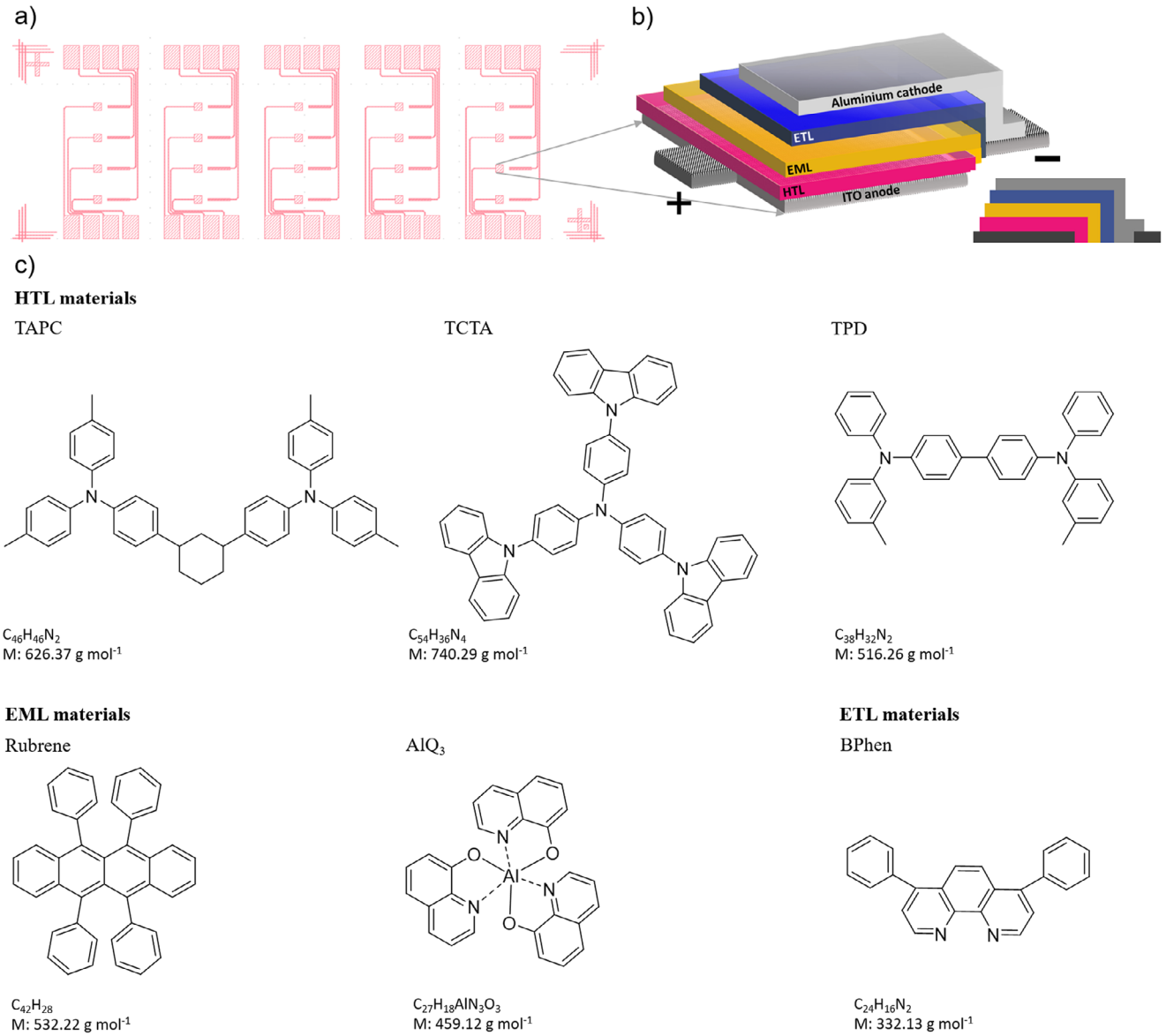

FIGURE 4 | a) Schematic 2D layout of the structured ITO slide, featuring 20 ITO squares, each measuring 1 mm^2, designated as printing regions. These squares are connected to contact pads along the edges to facilitate attachment of connection legs. b) A conceptual 3D representation of the printed devices shows OLEDs fabricated on the structured ITO, with each successive layer reduced in size to prevent unwanted overlap. On the right, the structures were extended to minimize the risk of short-circuiting between the aluminum cathode and the ITO layer. c) Chemical structures of the materials used for OLED fabrication by LIFT printing.

TABLE 1 | Transfer parameters of each material used to print OLEDs.

Material	Concentration [$mgmL^{-1}$]	Laser power [mW]	Exposure [ms]	Prints	Type of Polyimide
TCTA	30	70	3	2x	Flexiso PI FI 16125
TPD	30	70	2	1x	Flexiso PI FI 16125
Rubrene	8	70	2	1x	CMC Klebetechnik 70110
Alq_3	15	70	2	1x	Flexiso PI FI 16125
Bphen	4	70	2	1x	CMC Klebetechnik 70110

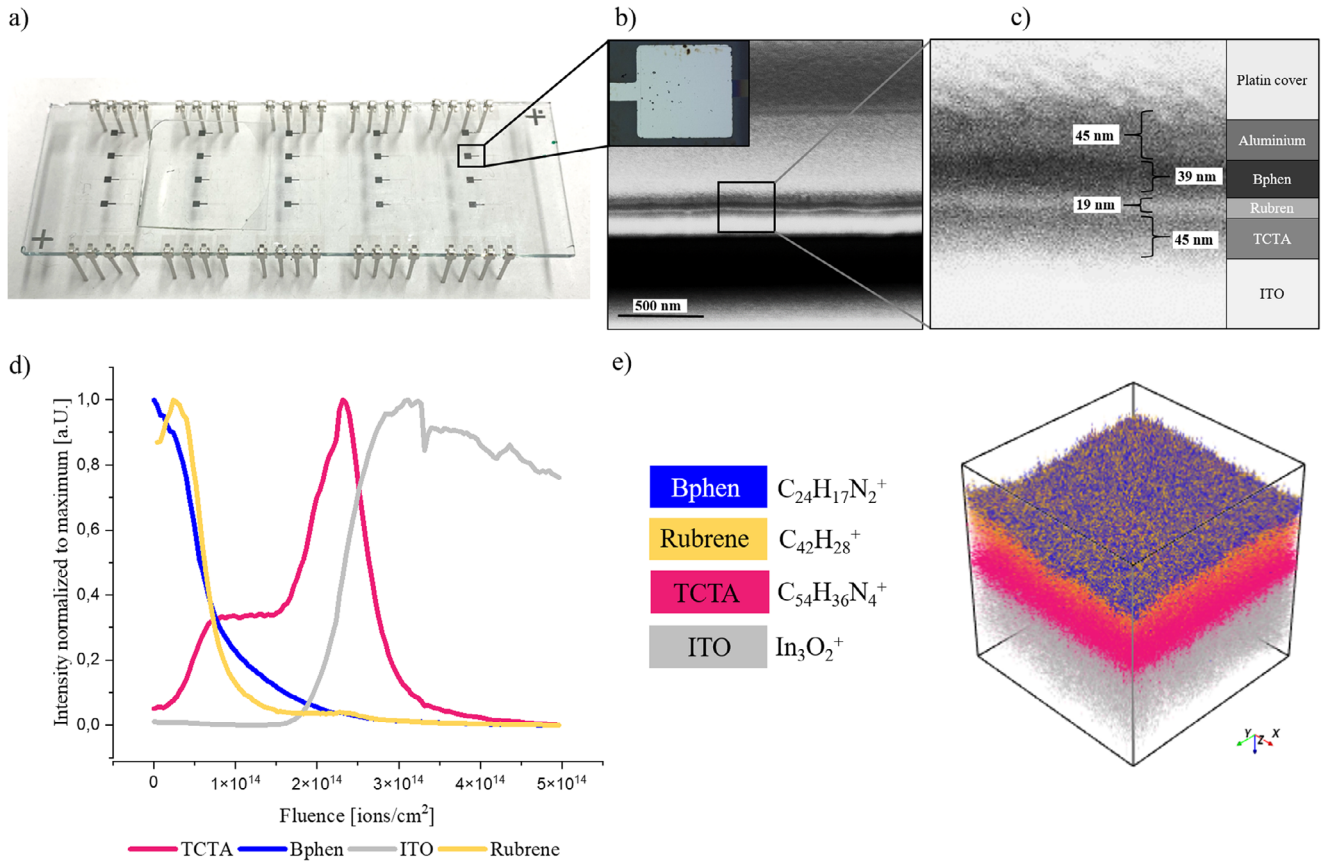

FIGURE 5 | a) Overview of the OLED sample, including connection legs, after the printing and deposition of the Al cathode. b) Light microscopic image of an individual OLED device and SEM cross-section image of a typical printed OLED, highlighting the layer architecture: glass substrate, ITO, TCTA, Rubrene, Bphen, aluminum, and a protective platinum layer deposited during FIB-SEM preparation. c) High-resolution SEM cross-section image of a typical printed OLED, showing emission. Variations in gray values indicate material contrast between different layers. d) ToF-SIMS depth profile of the different molecule ion peaks illustrating the layer sequence of the OLED structure. e) 3D reconstruction of the depth profile obtained by ToF-SIMS of a representative OLED (Signals integrated from a field of view of 300 μm × 300 μm in x and y, z not to scale.).

To identify the most promising material stack, various constellations of EML and HTL materials were investigated, while keeping the cathode, anode and ETL constant. The functionality of the printed OLEDs was evaluated using the MATIS System (see Supporting Information) by evaluating emission, current, and current stability of the system. OLEDs were classified as functional if emission was detected by the spectrometer. The printing of stable and working OLEDs with LIFT was successfully demonstrated using the combinations of material of the HTL materials TCTA and TPD, along with the emitter materials Rubrene and Alq_3, in combination with the ETL material BPhen. The printed components were characterized by their electrical and optical properties. Among these configurations the combination of ITO–TCTA–Rubrene–BPhen–Aluminum demonstrated superior printability, structural integrity and overall device reliability. As a result, this particular OLED setup was selected for detailed characterization.

Figure 5 shows an array of 20 printed OLEDs on a glass slide based on this optimized architecture. FIB analysis was carried out to evaluate the structure and quality of the layer-by-layer architecture by obtaining cross-sectional views. SEM image and zoomed-in view (Figure 5) show material contrast across the printed layers, visible as differences in brightness. The bottom layer corresponds to the glass substrate, followed by the ITO electrode and the successively deposited organic layers. The measured layer thicknesses, more clearly visible in the zoomed-in view of the cross-section in Figure 5c, were: TCTA – 45 nm, Rubrene – 19 nm, BPhen – 39 nm, and aluminum – 45 nm. A platinum capping layer was added on top solely for protection purposes. The deposited layers exhibit a predominantly parallel alignment with deviations of only a few nanometers. The interfaces appear continuous and free of delamination or voids, indicating high-quality printing and material compatibility. To provide deeper insights and prove the integrity of the transferred material, ToF-SIMS measurements were additionally conducted. Figure 5d shows an in-depth profile of an OLED stack (ITO–TCTA–Rubrene–BPhen) representing an area of 300 × 300 μm^2, measured in positive ion mode. In this mode, intact molecule peaks for each layer were detectable, indicating the excellent stability of the OLED materials during the transfer process. The profile reveals that the first detected material corresponds to the ion peak of BPhen ($C_{24}H_{17}N_2^+$, blue), located at the surface. As the BPhen signal declines, a signal for Rubrene ($C_{42}H_{28}^+$, yellow) becomes more pronounced. The graphs of BPhen and Rubrene show the clear sequence of the layers but no distinct interface. At greater depths—indicated by higher fluence—TCTA ($C_{54}H_{36}N_4^+$, pink) is detected, showing a distinct interface by a

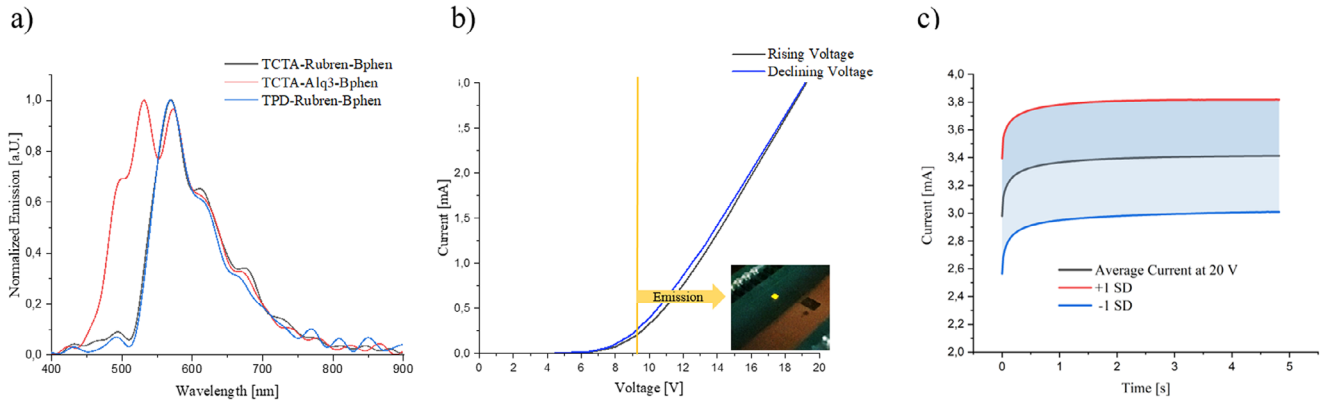

FIGURE 6 | a) Normalized electroluminescence spectra of various OLED types operated at 20 V, showing the detected wavelength distributions. b) Current-voltage (I–V) curve of an ITO-TCTA-Rubrene-Bphen-Aluminum OLED, measured during both increasing and decreasing voltage sweeps. c) Current stability over time for a single ITO-TCTA-Rubrene-BPhen-Aluminum OLED under constant operation for 5 s. The average current of seven devices is shown, with the standard deviation indicated.

clear increase in the intensity of the related ion peaks, followed by a plateau in intensity while the other ion peaks vanish. The intensity plateau of TCTA is followed by a second increase in signal, resulting from an interface effect near the ITO ($In_3O_2^+$, gray) layer, which causes an elevated ion count. For better visualization, the depth profile is depicted as a 3D reconstruction of the measured sample in Figure 5e. This representation shows the desired LbL structure. Also visible is an apparent intermixing effect between BPhen and Rubrene, which cannot be clearly assigned to the printing method but is likely an artefact of the sputter erosion process applied in the SIMS profile aquisition. Due to the signal integration across 300 µm × 300 µm field of view in xy, (see also Section 5.2.4) every local layer thickness deviation within this field of view is attributing to reduced interface fidelity. An undulated interface or a slightly skewed interface, as well as a skewed or otherwise uneven erosion front being rather unremarkable in SEM reduces the obtained depth resolution. These results demonstrate the potential of the LIFT technique for the fabrication of precise 3D multilayer structures, enabling the production of three-layer OLEDs by stacking various combinations of TPD, TCTA, Rubrene, Alq_3, and BPhen.

For an analysis of the optical emission of the functional stacks electrical contacts were applied and the emitted light was collected and fed into a spectrometer for detection. The normalized, qualitative electroluminescence spectra of working stacks are shown in Figure 6a. The material stack comprising TCTA or TPD with Rubrene and BPhen exhibited a broad emission peak with a maximum at approximately 570 nm. The emission peak looks similar to findings in the literature [42], even though the stack layout is not identical. Substituting Rubrene with Alq_3 resulted in a double peak at 530 nm and 580 nm. Tang et al. [43] mentioned the double peak as a result of recombinations from the triplet excitons or the presence of "defect states." Emission was detected over a time period of 5 s to 10 s, during which the OLEDs were continuously operated. OLED stacks of the layout TCTA–Rubrene–BPhen were tested for durability in terms of operational lifetime (under emission) and shelf lifetime, with intermediate tests of 10 s. For assessment of the operational lifetime, the OLEDs were continuously operated at 1.6 mA and 14.7 V with permanent emission for 20 min. A moderate decline in relative emission intensity was observed during the measurement (see Figure S2, Supporting Information).

Further tests for the shelf life showed that the overall span of non-encapsulated OLEDs operating under argon atmosphere was at least 9 days. A decline of relative emission intensity was observed until no more signal was detected. The measurements are described in more detail in the supplementary information. The yield of functional devices within a single batch of 20 OLEDs was approximately 12 out of 20, with functional devices defined as those for which emission could be detected.

To evaluate the electrical performance of the printed OLED, a current–voltage (I–V) curve was measured, as shown in Figure 6b. Below 7 V the current remained low before increasing almost linearly. Emissions could be observed at a turn-on voltage of 9 V and above. The voltage was raised to 20 V and subsequently reduced back to zero while the current was continuously measured. Only a small deviation between the rising and falling voltages was observed. The behavior appears similar to that of a conventional electrical diode [44]. To assess the temporal stability of the current in the printed OLEDs, time-dependent current measurements were performed, as shown in Figure 6c. The average current of seven devices exhibiting emission is presented, along with the corresponding standard deviation (devices that turned off during measurement were excluded). Initially, the current started at 3.0 mA and raised by approximately 10% to 3.2 mA, where it stabilized throughout the measurement period of 5 s. The standard deviation of the devices is approximately ± 12%, represented by the colored area in the plot. A changing current suggests internal processes within the OLED materials, potentially related to temperature adaptation or material degradation. Overall, the observed current stability indicates reliable operation of the printed OLED over the measurement period. Minor fluctuations in the current–voltage behavior may be attributed to intrinsic material properties and transient thermal effects, as observed in the long-term measurement shown in Figure S2 (Supporting Information). In some printed devices porosity was detected after the operation of the OLEDs, corresponding to areas within the pixel that lacked emission. Analysis under the microscope indicates that these areas are related to printing defects which can

occur in certain cases and may be caused by an inhomogeneous distribution of materials on the donor slide (see Figure S3, Supporting Information)

4 | Conclusion

We demonstrated that the localized transfer of homogeneous layers with adjustable thickness down to a few nanometers can be achieved using a novel LIFT printing technique. Vertical scanning interferometry was used to characterize the quality of the printed layers, revealing surface roughness values in the low nanometer range, depending on the transfer parameters. Notably, the lowest surface roughness (R_a) of 2.78 nm ± 0.25 nm was achieved for the printing of BPhen, which was also used for OLED fabrication. This minimal roughness is particularly beneficial for optoelectronic applications, as it directly influences layer uniformity and interface quality, both critical for device performance. The layer thickness can be tuned by varying the concentration of the coating solution on the donor slide or by adjusting the transfer parameters.

This capability enables the fabrication of complex devices such as OLEDs, which demand precise control over chemical composition, physical layer properties and interlayer characteristics. Thin material layers as well as structures that require lateral composition of different materials in precise geometry are possible. The thickness of layers fabricated by LIFT printing can be accurately controlled and can be adjusted via the concentration of the donors in the range of just a few nanometers, offering significant potential in the design of components and devices by screening for the ideal conditions.

The printed layers were successfully combined into multilayer stacks by successive printing. To demonstrate the quality of the transfer, the OLED stack TCTA-Rubrene-BPhen was characterized electrically and optically as well as by destructive methods such as FIB-SEM and ToF-SIMS. Functional OLEDs in this configuration, emitting light at approximately 580 nm, could be printed. The lifetime of the OLEDs was at least 20 minutes during continuous operation and 9 days if stored with intermediate testing.

Further optimization of the process could improve the yield and emission intensity of the devices. Additionally, gaining a deeper understanding of the mechanisms underlying the transfer process in this printing method would be beneficial, which will be the subject of future research. More complex OLED layouts with more than three layers could also be achieved using other material combinations. This printing technology provides the flexibility to create devices of various shapes and sizes and is not constrained by the production limitations of expensive lithographic masks.

5 | Materials and Methods

5.1 | Materials

In this study, various OLED materials were investigated, including tris(4-carbazoyl-9-ylphenyl)amine (TCTA), *N,N'*-Bis-(3-methylphenyl)-*N,N'*-diphenylbenzidine (TPD), 5,6,11,12-tetraphenylnaphthacene (Rubrene), tris-(8-hydroxychinolin)aluminum (Alq_3), bathophenanthrolin (BPhen) and styrene acrylic copolymer S-LEC PLT 7552, (SEKISUI, Japan).

Two types of polyimide tape were employed as donor films for printing, as they behave slightly differently for the transfer because of their absorption behavior and material properties: (1) brown polyimide adhesive tape (CMC Klebetechnik, 70110 brown) with a thickness of 25 µm, and (2) black polyimide adhesive tape (Dr. Dietrich Müller GmbH, Flexiso PI FI 16125 schwarz) with a thickness of 25 µm. The observed greater material expansion suggests a higher laser absorption in the black polyimide compared to the orange variant, which would consequently result in an elevated transfer temperature. Depending on the transfer material, one of the two polyimide types was favored over the other.

5.2 | Methods

5.2.1 | Printer Setup

Our BA-LIFT setup is custom built and uses a 405 nm diode laser (iBeam smart 405-S, TOPTICA Photonics AG, Munich, Germany) with a maximum power output of 300 mW in combination with a two-mirror laser scan head (intelliSCAN III 10, SCANLAB GmbH, Puchheim, Germany) for localized transfer of material. An F-Theta lens (JENar 170-355-140; JENOPTIK Optical Systems GmbH, Jena, Germany) was used to focus the collimated laser beam onto the donor slide. The laser energy is absorbed by the polyimide film of the donor slide, causing it to expand. This expansion is driven by the blister formation of hot gases, which creates a contact between the transfer material and the acceptor slide. This specific transfer process was closely investigated by Paris et al. [34] using an almost identical setup. In addition to the previously described components, a heating and cooling system was installed in the stage onto which the acceptor substrate is clamped to maintain stable transfer conditions. The setup temperature was monitored and maintained at 21 °C. A spacer with a thickness of 10 µm, made of steel sheet metal, was placed between the donor and acceptor slides to ensure consistent spacing.

5.2.2 | Preparation of the Donor Slide

Before printing, the donor slides were prepared using microscope glass slides measuring 76 mm × 26 mm (Paul Marienfeld GmbH & Co. KG, Germany). These glass slides were first covered with adhesive polyimide tape (orange: CMC Klebetechnik GmbH, Frankenthal, Germany; black: Dr. Dietrich Müller GmbH, Flexiso PI FI 16125) before being blade-coated with a transfer material solution. The solution was prepared by dissolving material powders in organic solvents such as chloroform or dichloromethane. All material powders were soluble in both solvents except TCTA, which requires pure chloroform. Donor coatings were applied using an automated film applicator (TQC Sheen), which moved a blade along the length of the glass slide. The blade was set to a height of 1500 µm and moved at a speed of 10 mms^{-1}, evenly distributing 60 µL of solution across the slide.

5.2.3 | Printing of OLEDs

5.2.3.1 | Substrate Preparation:. For the fabrication of printing substrates, ITO glass substrates measuring 75 mm × 25 mm (Ossila B.V., Leiden, NL) were used. The fabrication of microstructures on ITO-coated glass substrates begins with the deposition of a positive photoresist (ma-N 1420) via spin-coating at 3000 rpm for 60 s, followed by a pre-exposure bake at 110 °C for 2 min to optimize adhesion. The substrates are then exposed to 135 mJ cm^{-2} ultraviolet light using a mask and developed for 4.5 min using ma-D 5335 developer to reveal the ITO layer underneath. The etching of unprotected ITO areas is conducted by immersing the slides in a 4.0M HCl solution for 50 min in a temperature-controlled water bath maintained at 30 °C. Any remaining photoresist is stripped using an acetone/isopropyl solution, followed by a rinse with deionized water.

5.2.3.2 | Printing of the Shifted Pyramid Layout OLED:. OLEDs were printed using different combinations of HTL materials (TCTA and TPD) and emitters (Rubrene and Alq_3) in conjunction with the ETL material BPhen. To achieve the pyramid layout, the bottom layer was printed as a rectangle consisting of 165 by 190 dots with a pitch of 8 μm. This resulted in a rectangular surface measuring 1320 μm × 1520 μm. The second layer was reduced by 40 μm on each side, except on the side with the ITO track of the cathode where it was extended by 40 μm. Similarly, the third layer was reduced by another 40 μm on each side and extended by 40 μm on the cathode side. At the top of the pyramid the evaporated aluminum cathode formed a square measuring 1000 μm on each side with an elongation of 1100 μm in length and 200 μm in width toward the cathode. This printing layout was kept for all tested material combinations. After printing, the aluminum cathode was deposited via evaporation. A shadow mask was manually positioned on the acceptor slide using a light microscope. To prevent damage to the structures, a polyimide tape spacer was placed between the acceptor slide and the mask. Aluminum, with a thickness of approximately 100 nm, was evaporated using an evaporator (UNIVEX 400 Leybold). Process parameters were 0.1 nms^{-1} with no tilt and a rotation of the sample with 10 rpm. The sample was kept at 20 °C and at 8.0×10^{-6} bar during the evaporation.

5.2.4 | Characterization

5.2.4.1 | Vertical Scanning Interferometry. For optical and topographical characterization a VSI Contour GT-KOX-14-157 from Bruker (Ettlingen, Germany) was employed. The system enables non-contact, high-resolution surface profiling by capturing three-dimensional topographical data with nanometer precision. Measurements were typically performed at 2.5x magnification unless stated otherwise, and data analysis was carried out using Vision64 software. VSI is particularly well-suited for rapid surface characterization, providing detailed insights into surface roughness, layer thickness and microstructural features, making it an essential tool in material science and microfabrication.

5.2.4.2 | Scanning Electron Microscopy. FIB-SEM characterization was performed on an FEI DualBeam Helios G4 FX (Thermo Fisher Scientific) which enables simultaneous focused ion beam milling and high-resolution electron imaging. The OLED samples were prepared using standard mounting procedures and were milled using a gallium ion source to expose cross-sectional views of the printed structures. To prevent beam-induced damage and ensure clean trench edges, a protective platinum layer was deposited in situ from a precursor gas prior to milling. Following trench preparation the sample stage was tilted by 52 ° to acquire high-contrast cross-sectional SEM images using the integrated secondary electron detector.

5.2.4.3 | Time-of-Flight Secondary Ion Mass Spectrometry (ToF-SIMS). ToF-SIMS was performed on a TOF.SIMS 5 instrument (ION-TOF GmbH, Münster, Germany). This spectrometer is equipped with a Bi liquid cluster primary ion source and a reflection type time-of-flight analyzer. UHV base pressure was $< 5 \times 10^{-8}$ mbar. For high mass resolution the Bi source was operated in the "high current bunched" mode providing 1.24 ns Bi_3^+ primary ion pulses at 25 keV energy, a lateral resolution of approximately 4 μm and a target current of 0.35 pA at 100 μs cycle time. The primary ion beam was scanned across a 300 × 300 μm^2 field of view on the sample and 128 × 128 data points were recorded. Spectra were calibrated on the omnipresent C^+, CH^+, CH_2^+, and $C_2H_2^+$, Sn^+ and InO_3^+ peaks. Based on these datasets, the chemical assignments for characteristic fragments were determined. For depth profiling a dual beam analysis was performed in non-interlaced mode. The sputter gun, operated with Ar_{1300}^+ ions at 2.5 keV scanned over a concentric field of 750 × 750 μm^2 with a target current of 0.62 nA, was applied to erode the sample. The primary ion beam was scanned across a 300 × 300 μm^2 field of view centered in the crater, and 128×128 data points were recorded with a target current of 0.28 pA to 0.35 pA at 100 μs cycle time. The shift of the calibration due to charging effects during the depth profiling was corrected using advanced ToF correction (depth) of the onboard software.

5.2.4.4 | Optical and Electrical Characterization. For optical and electrical characterization a Modular Automated Testing and Inspection System (MATIS) was used [45]. The system features a four-axis platform with an XY-stage and vacuum chuck to hold the sample carrier. A gantry-mounted probe head with a Thorlabs F950SMA-A lens collects emitted light which is transmitted via a 2 m UV-Vis fiber (400 μm core) to an Ocean Optics USB650 spectrometer. Electrical contact is established through ZIF sockets integrated into a PCB with multiplexed relay control, enabling individual OLED addressing. A Keithley 2612b SMU supplies current (I_{max} = 10 mA, V_{max} = 20 V) and records electrical performance. During measurements the OLEDs face downward and the emitted light is collected from above. An argon atmosphere protects unencapsulated devices from degradation. Spectra are acquired either manually or in semi-automated mode via position teach-in with fiducial recognition. Data smoothing was performed for the acquired spectra using a low-pass filter with a cutoff frequency of 0.03 Hz. Further details of the setup are provided in Figure S1 (Supporting Information).

Acknowledgements

The authors acknowledge the support from the EU under the NANOSTACKS project EXCELLENT SCIENCE - Future and Emerging

Technologies (FET) (ID: 951949) for financial support. The authors acknowledge support from the Deutsche Forschungsgemeinschaft (DFG) under Germany's Excellence Strategy - 3DMM2O (EXC-2082/1-390761711). We further acknowledge support from the Helmholtz Society's program Materials Systems Engineering, in the Research Area Information (43.35.03). The authors appreciate financial support by the KIT-Publication Fund. Thanks are due to Christian Rainer for structuring the ITO and Richard Thelen for his support in the labs. All authors contributed to the revision of the manuscript.

Open access funding enabled and organized by Projekt DEAL.

Conflicts of Interest

Frank Breitling declares a possible conflict of interest regarding being shareholder of the company PEPperPRINT GmbH, Heidelberg which uses the LIFT system for peptide array production.

Data Availability Statement

The data that support the findings of this study are openly available in KIT open at https://doi.org/10.35097/y1bdr10s23qa3ny3, reference number 1000182107.

References

1. A. Piqué, D. B. Chrisey, R. C. Y. Auyeung, et al., "A Novel Laser Transfer Process for Direct Writing of Electronic and Sensor Materials," *Applied Physics A* 69, no. 1 (1999): S279–S284, https://doi.org/10.1007/s003390051400.

2. "Surface Mount Technology: Principles and Practice | Springerlink," https://link.springer.com/book/10.1007/978-94-011-6532-7 (2025), accessed May 7, 2025.

3. N. A. Kyerematen, T. Brousse, and D. Pech, "Microsupercapacitors as Miniaturized Energy-Storage Components for On-Chip Electronics," *Nature Nanotechnology* 12, no. 1 (Nov. 2016): 7–15, https://doi.org/10.1038/nnano.2016.196.

4. A. H. Espera, J. R. C. Dizon, Q. Chen, and R. C. Advincula, "3d-Printing and Advanced Manufacturing for Electronics," *Progress in Additive Manufacturing* 4, no. 3 (Feb. 2019): 245–267, https://doi.org/10.1007/s40964-019-00077-7.

5. D. Han and H. Lee, "Recent Advances in Multi-Material Additive Manufacturing: Methods and Applications," *Current Opinion in Chemical Engineering* 28 (June 2020): 158–166, https://doi.org/10.1016/j.coche.2020.03.004.

6. Z. Huang, G. Shao, and L. Li, "Micro/Nano Functional Devices Fabricated by Additive Manufacturing," *Progress in Materials Science* 131 (Jan. 2023): 101020, https://doi.org/10.1016/j.pmatsci.2022.101020.

7. J. Perelaer, P. J. Smith, D. Mager, et al., "Printed Electronics: The Challenges Involved in Printing Devices, Interconnects, and Contacts Based on Inorganic Materials," *Journal of Materials Chemistry* 20 (2010): 8446–8453, https://doi.org/10.1039/C0JM00264J.

8. O. Pabst, J. Perelaer, E. Beckert, U. S. Schubert, R. Eberhardt, and A. Tünnermann, "All Inkjet-Printed Piezoelectric Polymer Actuators: Characterization and Applications for Micropumps in Lab-On-A-Chip Systems," *Organic Electronics* 14, no. 12 (2013): 3423–3429, https://www.sciencedirect.com/science/article/pii/S1566119913003996.

9. A. Moya, G. Gabriel, R. Villa, and F. Javier del Campo, "Inkjet-Printed Electrochemical Sensors," *Current Opinion in Electrochemistry* 3, no. 1 (2017): 29–39, https://www.sciencedirect.com/science/article/pii/S2451910317300376.

10. M. Gao, L. Li, and Y. Song, "Inkjet Printing Wearable Electronic Devices," *Journal of Materials Chemistry C* 5 (2017): 2971–2993, https://doi.org/10.1039/C7TC00038C.

11. C. H. Rao, K. Avinash, B. K. S. V. L. Varaprasad, and S. Goel, "A Review on Printed Electronics with Digital 3D Printing: Fabrication Techniques, Materials, Challenges and Future Opportunities," *Journal of Electronic Materials* 51, no. 6 (Apr. 2022): 2747–2765, https://doi.org/10.1007/s11664-022-09579-7.

12. J. Lemarchand, N. Bridonneau, N. Battaglini, et al., "Challenges, Prospects, and Emerging Applications of Inkjet-Printed Electronics: A Chemist's Point of View," *Angewandte Chemie International Edition* 61, no. 20 (Mar. 2022), https://doi.org/10.1002/anie.202200166.

13. N. Mkhize and H. Bhaskaran, "Electrohydrodynamic Jet Printing: Introductory Concepts and Considerations," *Small Science* 2, no. 2 (2022): 2100073, https://onlinelibrary.wiley.com/doi/abs/10.1002/smsc.202100073.

14. A. Das, A. Ghosh, S. Chattopadhyaya, and C.-F. Ding, "A Review on Critical Challenges in Additive Manufacturing via Laser-Induced Forward Transfer," *Optics and Laser Technology* 168 (2024): 109893, https://www.sciencedirect.com/science/article/pii/S0030399223007867.

15. P. Serra and A. Piqué, "Laser-Induced Forward Transfer: Fundamentals and Applications," *Advanced Materials Technologies* 4, no. 1 (2019): 1800099, https://onlinelibrary.wiley.com/doi/abs/10.1002/admt.201800099.

16. S. Lux, N. Kuznetsova, A. R. Simha, D. Mager, F. Breitling, and J. G. Korvink, "Dot-By-Dot Printing of Capacitors by Lift," *Applied Research* 4, no. 1 (2025): e202400266, https://onlinelibrary.wiley.com/doi/abs/10.1002/appl.202400266.

17. B. Hopp, T. Smausz, G. Szabo, et al., "Femtosecond Laser Printing of Living Cells Using Absorbing Film-Assisted Laser-Induced Forward Transfer," *Optical Engineering* 51 (Jan. 2012): 014302.

18. A. Das and C. Ding, "Innovative Fabrication of Metal Alloy Structures via Laser-Induced Forward Transfer on Flexible Substrates," *Small Methods* 8, no. 9 (Dec 2023), https://doi.org/10.1002/smtd.202301429.

19. P.-P. Liu, S.-F. Lau, and C.-F. Ding, "Non-Enzymatic Low-Level Glucose Detection Electrode Fabricated via Single-Step Laser-Induced Forward Transfer," *Journal of Materials Chemistry A* 13, no. 1 (2025): 573–586, https://doi.org/10.1039/D4TA05603E.

20. Y. Liu, T. Knaus, Z. Wei, et al., "Confined Flash Printing and Synthesis of Stable Perovskite Nanofilms Under Ambient Conditions," *Advanced Materials* 36, no. 46 (Sept. 2024), https://doi.org/10.1002/adma.202409592.

21. S. Ronneberger, J. Zhang, Y. Liu, and F. F. Loeffler, "Solid Ink Laser Patterning for High-Resolution Information Labels with Supervised Learning Readout," *Advanced Functional Materials* 33, no. 17 (Feb. 2023), https://doi.org/10.1002/adfm.202210116.

22. J. Zhang, R. Tan, Y. Liu, et al., "Printed Smart Devices for Anti-Counterfeiting Allowing Precise Identification with Household Equipment," *Nature Communications* 15, no. 1 (Feb. 2024), https://doi.org/10.1038/s41467-024-45428-3.

23. A. Tsouka, Y. Fu, M. G. Ricardo, et al., "Synthetic High-Throughput Microarrays of Peptidoglycan Fragments as a Novel Sero-Diagnostic Tool for Patient Antibody Profiling," *Angewandte Chemie International Edition* (Feb. 2025), https://doi.org/10.1002/anie.202420874.

24. J. Moreno-Labella, R. Candorcio-Simón, D. Munoz-Martin, S. Lauzurica, M. Morales, and C. Molpeceres, "Blister-Actuated Laser-Induced Forward Transfer (Ba-Lift): Understanding Blister Dynamics for Enhanced Process Control," *Optics & Laser Technology* 182 (Apr. 2025): 112087, https://doi.org/10.1016/j.optlastec.2024.112087.

25. F. Chen, J. Bian, J. Hu, et al., "Mass Transfer Techniques for Large-Scale and High-Density Microled Arrays," *International Journal of Extreme Manufacturing* 4, no. 4 (Nov. 2022): 042005, https://doi.org/10.1088/2631-7990/ac92ee.

26. M. S. Kim, J. An, J. H. Lee, et al., "Clinical Validation of Face-Fit Surface-Lighting Micro Light-Emitting Diode Mask for Skin Anti-Aging Treatment," *Advanced Materials* 36, no. 50 (2024): 2411651, https://advanced.onlinelibrary.wiley.com/doi/abs/10.1002/adma.202411651.

27. R. Fardel, M. Nagel, F. Nüesch, T. Lippert, and A. Wokaun, "Fabrication of Organic Light-Emitting Diode Pixels by Laser-Assisted Forward

Transfer," *Applied Physics Letters* 91, no. 6 (Aug. 2007), https://doi.org/10.1063/1.2759475.

28. J. Shaw Stewart, T. Lippert, M. Nagel, F. Nüesch, and A. Wokaun, "Red-Green-Blue Polymer Light-Emitting Diode Pixels Printed by Optimized Laser-Induced Forward Transfer," *Applied Physics Letters* 100, no. 20 (May 2012): 203303, https://doi.org/10.1063/1.4717463.

29. J. R. H. Shaw-Stewart, T. Mattle, T. K. Lippert, M. Nagel, F. A. Nüesch, and A. Wokaun, "The Fabrication of Small Molecule Organic Light-Emitting Diode Pixels by Laser-Induced Forward Transfer," *Journal of Applied Physics* 113, no. 4 (Jan. 2013): 043104, https://doi.org/10.1063/1.4788710.

30. J. R. H. Shaw-Stewart, T. K. Lippert, M. Nagel, F. A. Nüesch, and A. Wokaun, "Sequential Printing by Laser-Induced Forward Transfer to Fabricate a Polymer Light-Emitting Diode Pixel," *ACS Applied Materials & Interfaces* 4, no. 7 (2012): 3535–3541, https://doi.org/10.1021/am300598h.

31. C. Constantinescu, A. Diallo, L. Rapp, et al., "Laser-Induced Forward Transfer of Multi-Layered Structures for OTFT Applications," *Applied Surface Science* 336 (2015): 11–15, e-MRS 2014 Spring Meeting. Symposium J. Laser Interaction with Advanced Materials: Fundamentals and Applications, https://www.sciencedirect.com/science/article/pii/S0169433214014731.

32. N. T. Kattamis, N. D. McDaniel, S. Bernhard, and C. B. Arnold, "Laser Direct Write Printing of Sensitive and Robust Light Emitting Organic Molecules," *Applied Physics Letters* 94, no. 10 (Mar. 2009): 103306, https://doi.org/10.1063/1.3098375.

33. N. T. Kattamis, P. E. Purnick, R. Weiss, and C. B. Arnold, "Thick Film Laser Induced Forward Transfer for Deposition of Thermally and Mechanically Sensitive Materials," *Applied Physics Letters* 91, no. 17 (Oct. 2007): 171120, https://doi.org/10.1063/1.2799877.

34. G. Paris, A. Klinkusch, J. Heidepriem, et al., "Laser-Induced Forward Transfer of Soft Material Nanolayers with Millisecond Pulses Shows Contact-Based Material Deposition," *Applied Surface Science* 508 (2020): 144973, https://www.sciencedirect.com/science/article/pii/S0169433219337900.

35. F. F. Loeffler, T. C. Foertsch, R. Popov, et al., "High-Flexibility Combinatorial Peptide Synthesis with Laser-Based Transfer of Monomers in Solid Matrix Material," *Nature Communications* 7 (2016): 11844.

36. D. Munoz-Martin, C. Brasz, Y. Chen, M. Morales, C. Arnold, and C. Molpeceres, "Laser-Induced Forward Transfer of High-Viscosity Silver Pastes," *Applied Surface Science* 366 (Mar. 2016): 389–396, https://doi.org/10.1016/j.apsusc.2016.01.029.

37. E. Turkoz, L. Deike, and C. B. Arnold, "Comparison of Jets from Newtonian and Non-Newtonian Fluids Induced by Blister-Actuated Laser-Induced Forward Transfer (Ba-Lift)," *Applied Physics A* 123, no. 10 (Sept. 2017), https://doi.org/10.1007/s00339-017-1252-3.

38. S. Eickelmann, S. Ronneberger, J. Zhang, G. Paris, and F. F. Loeffler, "Alkanes as Intelligent Surface Thermometers: A Facile Approach to Characterize Short-Lived Temperature Gradients on the Micrometer Scale," *Advanced Materials Interfaces* 8, no. 3 (2021): 2001626, https://onlinelibrary.wiley.com/doi/abs/10.1002/admi.202001626.

39. D. Munoz-Martin, Y. Chen, M. Morales, and C. Molpeceres, "Overlapping Limitations for Ps-Pulsed Lift Printing of High Viscosity Metallic Pastes," *Metals* 10, no. 2 (2020), https://www.mdpi.com/2075-4701/10/2/168.

40. A. Das, D. Ghosh, S.-F. Lau, P. Srivastava, A. Ghosh, and C.-F. Ding, "A Critical Review of Process Monitoring for Laser-Based Additive Manufacturing," *Advanced Engineering Informatics* 62 (Oct. 2024): 102932, https://doi.org/10.1016/j.aei.2024.102932.

41. C. W. Tang and S. A. VanSlyke, "Organic Electroluminescent Diodes," *Applied Physics Letters* 51, no. 12 (Sept. 1987): 913–915, https://doi.org/10.1063/1.98799.

42. S. Engmann, A. Barito, E. Bittle, N. Giebink, L. Richter, and D. Gundlach, "Higher Order Effects in Organic Leds with Sub-Bandgap Turn-On," *Nature Communications* 10 (Jan. 2019).

43. H. Tang, H. Liao, K. Xu, Z. Zhou, and L. Zhu, "Two Peaks Observed in the Electroluminescence Spectra of Alq3-Based Oleds," *Journal of Luminescence* 118, no. 1 (May 2006): 39–44, https://doi.org/10.1016/j.jlumin.2005.06.009.

44. M. M. Rahman, N. Ogawa, Y. Miyazaki, Y. Nakayama, Y. Noguchi, and H. Ishii, "Time-Of-Flight Technique to Examine Carrier Blocking Nature in Organic Light Emitting Diode," *e-Journal of Surface Science and Nanotechnology* 10, no. 0 (2012): 315–320, https://doi.org/10.1380/ejssnt.2012.315.

45. L. Koker, K.-M. Reichert, U. Gengenbach, M. Reischl, and M. Ungerer, "Modular Platform for Automated Characterisation of Printed Structures, Devices and Circuits," in *2024 Symposium on Design, Test, Integration and Packaging of MEMS/MOEMS (DTIP)* (2024), 1–6.

Supporting Information

Additional supporting information can be found online in the Supporting Information section.

Supporting Information